DESIGN OF 10 MW LOW INDUCTANCE PM GENERATOR FOR DIRECT DRIVE OFFSHORE WIND TURBINE

BY

SIRIMANNA WITHANAGE DON THUSARA SAMITH SIRIMANNA

THESIS

Submitted in partial fulfillment of the requirements
for the degree of Master of Science in Electrical and Computer Engineering
in the Graduate College of the
University of Illinois at Urbana-Champaign, 2020

Urbana, Illinois

Adviser:

Associate Professor Kiruba Sivasubramaniam Haran

ABSTRACT

Direct drive permanent magnet synchronous generators (PMSG) in wind turbine applications are becoming increasingly popular due to their reliability compared to medium speed generators with a gearbox. A proposed generator-drive scheme with reduced active switching provides a way to reduce the power electronics cost significantly. This requires the per unit reactance (X_{pu}) of the generator to be low compared to conventional generators. Three PMSG topologies were designed, optimized and analyzed for their performance for this 10 MW direct drive generator-drive system. Optimization of these generator topologies for their efficiency and weight was performed. Comparisons between them for the efficiency, weight, X_{pu}, and cost are presented. Once the design is selected, integration of generator-drive system, challenges and results are also discussed and presented.

To my parents, for their love and support.

ACKNOWLEDGMENTS

I would like to thank ARPA-E for their funding of this research. I am thankful to my colleagues in the power and energy group at the University of Illinois Urbana-Champaign for their support in solving issues as they emerged.

Special thanks go to Dr. Dongsu Lee for his help in FEA related questions. Finally I want to thank my advisor Professor Kiruba Haran for his guidance on this research.

TABLE OF CONTENTS

CHAPTER 1

INTRODUCTION

1.1 Background of Modern Wind Generators

An increasing interest toward renewable energy is seen in recent history due to the increasing level of carbon emissions from fossil fuel. Among the renewable sources, wind turbines take a special place due to steady generation of power throughout the day. A large number of wind farms are in operation today, with wind generator units of 9.5 MW. Figure 1.1 shows the growth of turbine size over the time; from less than 2 MW designs up to 10 MW during the last four decades.

Increasing the power level of a turbine demands larger rotor blade sizes. Recent designs involving 10 MW wind turbines show rotor blades as large as 190 m. Large blade size limits the speed of rotation for the turbine due to noise limits, aerodynamic and mechanical considerations. A reference wind turbine proposed by Technical University of Denmark (DTU) provides a 10 MW baseline wind turbine design, taking in those considerations. It runs at a speed of 9.6 RPM [1]. This compares closely with the designs of commercial wind turbines in the same power range; with Windtec SeaTitan having a rated speed of 10 RPM and Shandong Swiss Electric having a rated speed of 9.45 RPM [2].

Generator design could take multiple directions based on the generator type and operating speed of the generator. Common generator types seen in this application are PMSG, doubly fed induction generator (DFIG) and wound rotor synchronous generator (WFSG). Figure 1.2 shows the generator type used on various power levels over time. The trend clearly shows the preference of PMSG toward the high power level. Based on whether or not a gearbox is used, operating speed of these machines varies from low speed (direct-drive) to medium speed or high speed generators. While high speed

generators are not seen at the 10 MW level, the medium speed solution with a gearbox is seen in commercial wind turbines. A medium speed generator enables smaller size compared to a direct drive generator. However, it introduces challenges related to possible failures in the gearbox. Direct-drive wind generators get rid of the problem, which is evidenced by many commercial manufacturers adopting the direct drive PMSG. However, the generator could be very large in size.

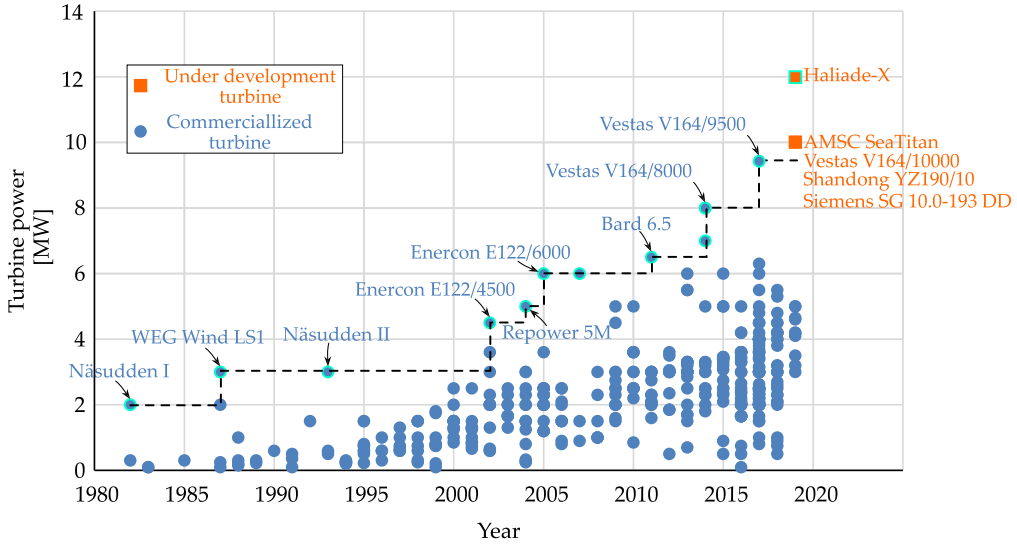

Figure 1.1: Evolvement of wind turbine power over time [2]

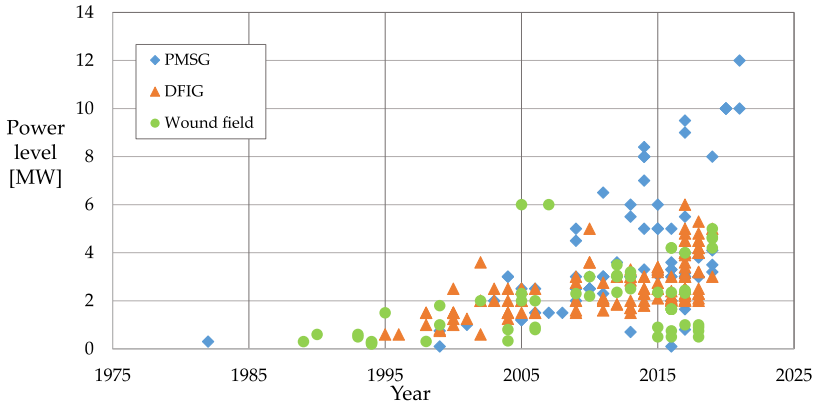

Figure 1.2: Generator types used at different power levels over time [2]

1.2 Proposed Drive Architecture

An integrated permanent magnet synchronous generator-rectifier architecture for limited speed range applications is proposed in [3]. A high level diagram for the proposed architecture is shown in Fig. 1.3. The generator consists of multiple three-phase ports where only one port is connected to an active rectifier while the remaining power is handled through diode bridge passive rectifiers. Proposed architecture can reduce the drive cost significantly compared to a fully rated drive due to reduced use of active rectifiers. The authors of [3] have shown the feasibility of this architecture on a lab setup by using a 160 W PMSG with 48 poles.

The main challenge in the proposed architecture is the current commutation in passive ports, which limits the power that can be handled by passive ports. This is a function of the inductance seen by the drive. This introduces the requirement for the inductance of the machine to be low compared to that of a conventional machine. Over the derivation, it has been shown that X_L^{pu} is the critical parameter to analyze, thus is used in place of inductance for the remainder of this thesis. Other implications include having to handle more power in the active port compared to passive ports and possible over-sizing of the active port windings in the generator. More details on implications by X_L^{pu} will be discussed in chapter 3.

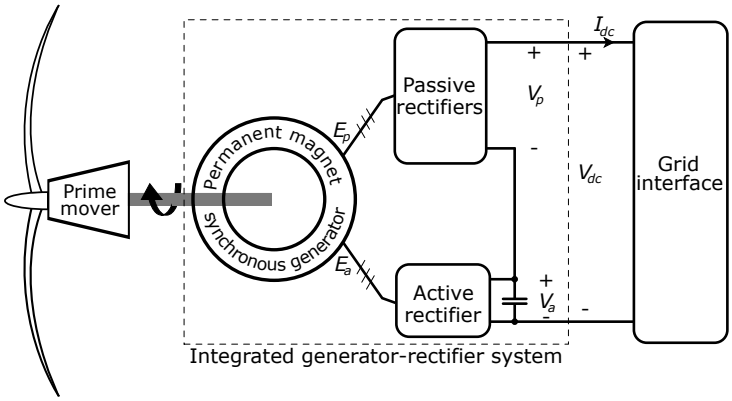

Figure 1.3: Proposed generator-drive architecture

1.3 Insights on Generator Design

Proposed generator-drive architecture considers X_L^{pu} to be a key parameter for integration. Thus, with the options available for different variations in stator, rotor designs, three PMSG topologies will be optimized for their efficiency and weight. Cost of the generators will be calculated based on materials used and it will provide a general idea on the feasibility of the topology.

Using a slotless stator and Halbach array permanent magnet (PM) rotor in PMSG has been shown to result in low inductance [4]. That is due to the lack of iron teeth in the stator and the increased effective airgap with no iron in the rotor yoke. That makes this generator architecture an interesting one to investigate for this application (topology I). Since a large quantity of rare-earth magnets are used in the direct drive, low speed high power wind generators, generator cost largely depends on PM cost. A comparison of the PM content and cost is shown in Fig. 1.4. Thus, a non-rare earth magnet PMSG was included as one of the topologies to explore (topology II). The conventional slotted PMSG with radial PM on the rotor is taken as the third topology (topology III).

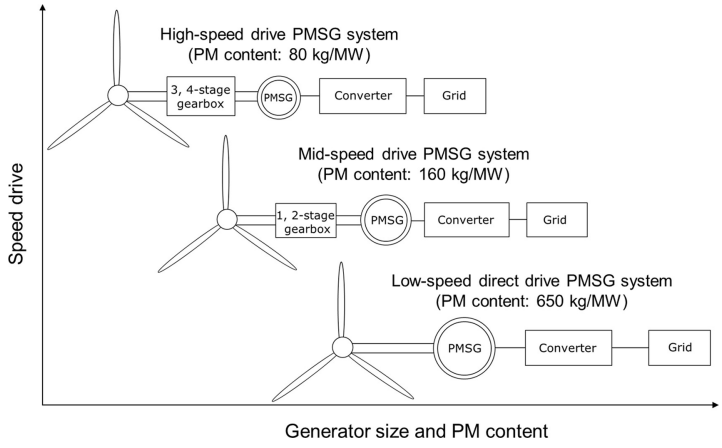

Figure 1.4: PM content and cost for wind generators [5]

A genetic algorithm based optimization scheme combined with finite element analysis (FEA) is carried out for the three generator topologies and results will be presented. Finally, for the selected topology, modeling and results of the effects due to power electronics integration is shown.

CHAPTER 2

GENERATOR DESIGN AND COMPARISON

2.1 Generator Specifications

Compared to a conventional generator design in wind-turbine applications, this generator is required to have a low X_L^{pu} for effectively delivering power through passive rectifiers. Thus, among the three suggested topologies, the generator with slotless stator, Halbach-array rotor of NdFeB permanent magnets is the most promising candidate. Thus, topology I will be investigated first.

Two soft targets for generator performance are set at rated efficiency of 97% and a torque density of 80 Nm/kg at rated power. Both efficiency and torque density targets are higher compared to the state-of-the-art direct drive wind generators.

Specifications for the generator design are based on a literature survey on existing high power wind generators and component availability for power electronics drive. Rated speed of 9.6 RPM with a rated output power of 10 MW and 3.3 kV voltage (rms line-line). A few other parameters were fixed for the study including pole number, maximum diameter, airgap length, and operating temperature.

Maximum generator diameter is an important parameter since these high power, low speed generators force the electric machines to reach for new regimes in machine design. For on-shore wind generators, size of the generator could be limited by logistics. However, off-shore wind generators with much larger diameters are seen in literature and industry. Few conceptual designs are available in [6, 7], which use generator diameters ranging approximately from 9-12 m. An industrial design by Enercon for a 4.6 MW wind generator is shown in [8], which has an airgap diameter of 10 m. A generator design for Dogger Bank reference wind farm is presented in [9] with 10 MW

generators of diameter 12 m. Thus, an outer diameter below 12.5 m will be used for this design.

Generator pole count is another design choice. Fundamental frequency is decided by the number of poles and rated shaft speed. A low fundamental frequency is preferred to minimize ripple current, which also demands a lower switching frequency for switching devices.

$$120\frac{f}{poles} = 9.6 \tag{2.1}$$

Now we consider the case with 120 poles, which results in a fundamental frequency of 9.6 Hz according to Eq. 2.1. Doubling the number of poles would make the fundamental frequency 19.2 Hz; however, it is still a relatively low frequency. Selection of fundamental frequency also affects the iron loss. However, as will be explained later, iron loss has a low contribution to overall losses in this low speed generator. Pole number selection also infers the length of a pole pitch. Figure 2.1 shows the pole-pitch geometry of the suggested generator topology.

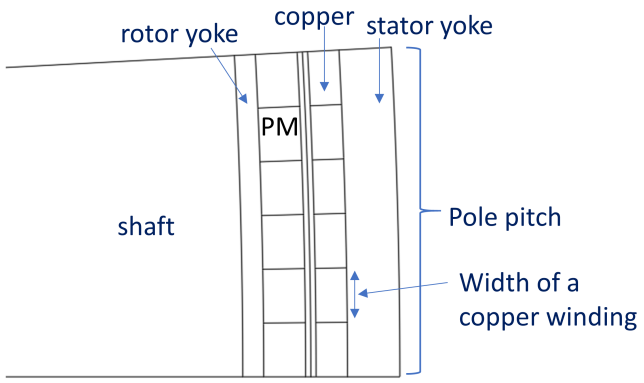

Figure 2.1: Geometry of a generator pole

A small pole pitch can reduce the end winding length, while also reducing the weight and copper loss in end windings. On the other hand, pole pitch length should be of a minimum manufacturable size. For an airgap diameter around 6 m, the pole pitch can be calculated as 130-150 mm. Literature provides comparable values for 10 MW wind generators [7]. Choosing two slots per-pole in the stator results in approximately 25 mm winding width. Dividing the rotor pole into six magnets with Halbach array suggests the

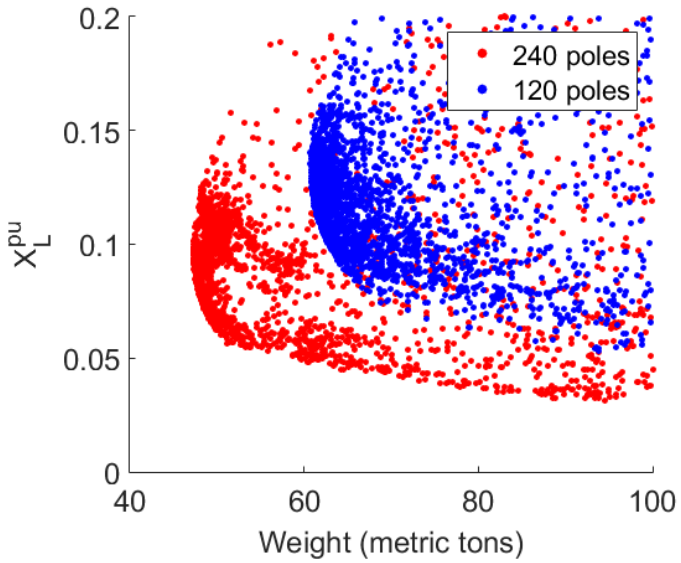

Figure 2.2: Difference in X_L^{pu} based on the number of poles

same width for magnets. From a manufacturing point of view, this is taken as a feasible value. The X_L^{pu} drops with increasing pole number as shown in Fig. 2.2. Thus, a trade-off exists between selecting a higher pole number and maintaining a manufacturable pole pitch. A 240-pole design was selected to meet both requirements. Thus the fundamental frequency of the generator will be 19.2 Hz.

The selection of airgap length depends on both thermal requirements as well as structural deflection level that can be allowed. In literature, many Mega-watt scale wind generators are found to have an airgap in the range of 10 mm [6, 7, 8]. Compared to high speed machines, this is a large airgap. However, 10 mm was selected, to accommodate a gravitational deflection of 10 % in airgap and to accommodate thermal expansion of the large structure.

A winding hotspot temperature below 155 °C is proposed based on the temperature gradient of an Enercon generator presented in [10]. Because of low-speed operation, iron and windage losses are expected to be relatively low for this generator. Thus, copper loss becomes the most significant loss component in evaluating efficiency. Selecting a lower operating temperature provides a better efficiency due to the reduced winding resistance. A temperature of 120 °C was considered for copper windings in calculating copper losses. A typical slot fill factor of 0.5 was assumed. Magnets are taken to operate at the same temperature, which gives the remanence flux density of

Table 2.1: Specifications and design choices

Parameter	Value
Rated power	10 MW
Rated speed	9.6 RPM
Rated voltage	3.3 kV (l-l)
Number of poles	240
Maximum diameter	12.5 m
Airgap	10 mm
Magnet B_r	1.2 T
Copper slot fill factor	0.5
Operating temperature	120 °C

NdFeB magnets to be 1.2 T.

A cost-effective non-grain-oriented silicon steel lamination material of M235-35A was selected for the stator yoke. It is an average performance material with saturation flux density close to 1.8. This selection has a minimum impact on iron losses due to the low fundamental frequency in this generator design. The gravimetric density of copper, NdFeB and M235-35A are inputs to the FEA model to calculate active generator weight. Specification and design choices in this generator design are summarized in Table 2.1.

Analytical modeling of slotless PM machines with an outer Halbach array rotor is described in [4]. This is implemented using the idea of magnetic vector potential, that relates to the airgap magnetic field. Tangential and radial magnetization vectors along the mechanical angle of the machine are discrete sinusoidal waveforms. Equations 2.2 and 2.3 can be used to evaluate the tangential fields at two surfaces (f,g) of Halbach array PM. Here, x_i are dimensions of the machine cross section, which includes the thickness of magnets, airgap, yoke and copper.

$$\begin{bmatrix} B_{\theta n}^{f} \\ B_{\theta n}^{g} \end{bmatrix} = \begin{bmatrix} F_0(x_i) & G_0(x_i) \\ G_0(x_i) & F_0(x_i) \end{bmatrix} \begin{bmatrix} A_z^f \\ A_z^g \end{bmatrix} - M_s \begin{bmatrix} X_s \\ Y_s \end{bmatrix} \tag{2.2}$$

where

$$M_s \ = \frac{j\mu_r\mu_0 npM_n}{(np)^2 - 1} \tag{2.3}$$

Here, p denotes the number of poles, n is the harmonic number, and M_n

represents the magnetization intensity of field magnets. X_0, Y_0 are functions of dimensional variables and F_0, G_0 components. After using boundary conditions on the surface of PM, resultant radial and tangential components of magnetic flux density can be obtained as a sinusoidal waveforms.

Analytical modeling of this architecture can be complex while the accuracy of the calculation can be limited. Thus, the study mainly focuses on an FEA based approach for the generator design.

2.2 Structural Considerations

Structural design includes two main considerations of maintaining the expansion and deflection levels. Analytical expressions given in Eq. 2.4 and Eq. 2.5 were used to calculate the structural expansion and deflection.

$$\epsilon_{thermal} = L_0 \Delta \mathrm{T} \alpha \tag{2.4}$$

where $\epsilon_{thermal}$ is the thermal expansion, L_0 is the original length, ΔT is the change in temperature, and α is material thermal expansion coefficient.

$$\epsilon_{gravity} = \frac{5}{384} \quad \frac{Wl^3}{EI} \tag{2.5}$$

where $\epsilon_{gravity}$ is the deflection due to gravity, W is the estimated total load, l is the shaft length between the two main bearings, E is the modulus of elasticity, and I is the moment of inertia. Expansion due to centrifugal force was calculated using the equations listed in [11]. The order-of-magnitude of thermal and gravity deflections were calculated to be 0.1 mm and 1 mm, respectively.

Figure 2.3 shows the integration method with turbine. The rotor will be connected to and supported by bearing outer race as shown, then connected to the turbine rotor. The stator will be connected to and supported by the main shaft, which is stationary. By properly sizing the inactive parts: shaft and rotor material, it is possible to control the deflection levels as necessary. However, given the feasibility of mechanical integration, this study will only focus on electromagnetic performance and active weight of the generator.

r

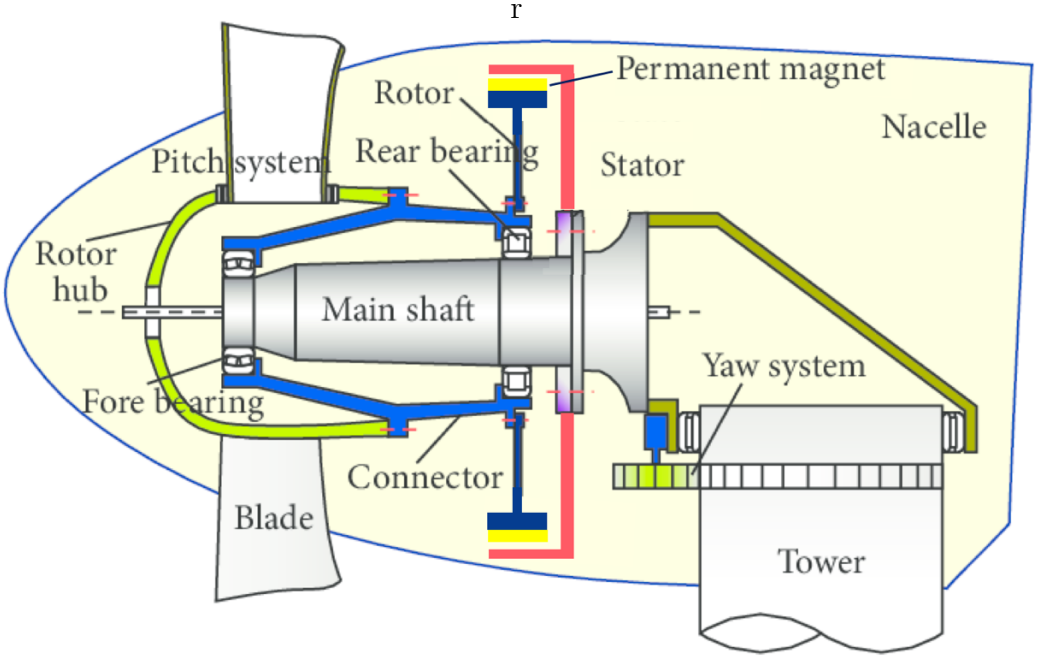

Figure 2.3: Structure and bearings modified from [12]

2.3 Thermal Considerations

A simple model of a one-dimensional thermal resistive circuit was developed for the generator stator. Equivalent thermal resistances were evaluated for each of the components accordingly. The simplified model gives access to quick calibration of the model for design changes. It assumes a liquid or a water cooled system to remove heat from within the generator.

Using the method given in [13], the thermal resistive circuit in Fig. 2.4 was developed to imitate the stator. Resistance of the airgap, copper windings, and stator yoke are calculated using the physical properties of the generator materials. Given the nature of this machine, a high percentage of losses will be generated in the stator. Using the thermal circuit, cooling system power was estimated to be in the range of few tens of kilowatts. In the generator electromagnetic design stage, thermal design will not be performed in detail. Instead, a fixed cooling power will be taken as an input to the efficiency calculations.

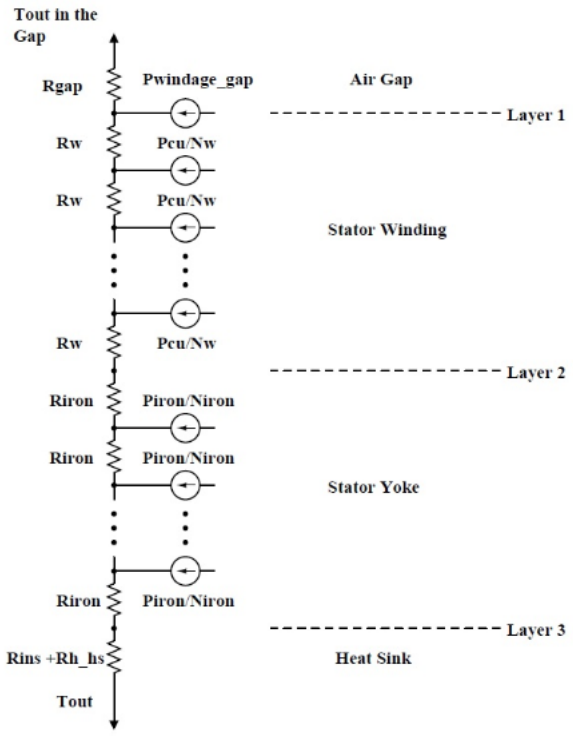

Figure 2.4: Equivalent thermal resistive circuit [13]

2.4 Generating Pareto Optimal Curves

A slotless generator with a Halbach array of rare-earth magnets in the rotor is shown in Fig. 2.5. It consists of a shaft, rotor yoke, PM, airgap, copper windings, and stator iron with materials properties assigned in FEA simulation. Use of the Halbach array eliminates the need to have an active material in the rotor yoke. Thus, the weight of the rotor yoke and shaft are not taken into account in the optimization process. Table 2.2 shows the lists of variables along with their constraints.

Table 2.2: Constraints used in optimization of generator topology I

Variable	Lower bound	Upper bound
Shaft radius X1 (mm)	5000	6000
Rotor yoke thickness X2 (mm)	30	200
Magnet thickness X3 (mm)	10	70
Copper thickness X4 (mm)	25	100
Stator yoke thickness X5 (mm)	10	60
Current density J (A/mm2)	1	4

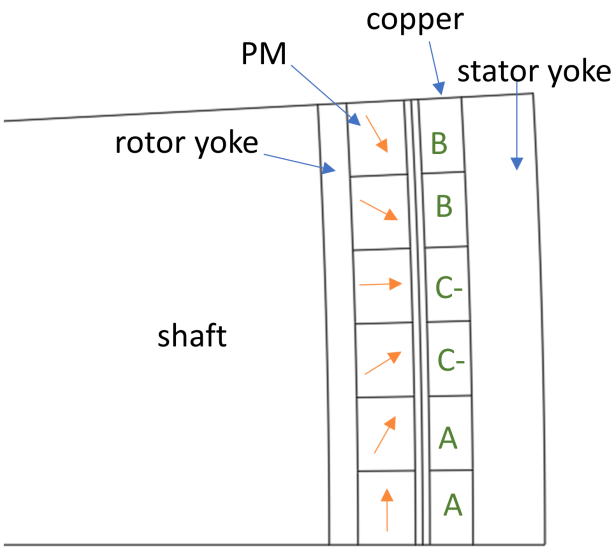

Figure 2.5: Geometric parameters used for optimization of generator topology I

Rated power and rated speed were defined in the specifications. Thus, the requirements for generator can be stated using the rated torque. This makes the objective for torque density is easy to calculate, as it is proportional to (1/weight). The second objective of efficiency is calculated using a combination of FEA and analytical methods, which will be discussed under the process. Creating the pareto optimal curve is done using an open source optimization algorithm, GOSET 2.6. This uses a MATLAB script to generate a set of variables based on the objective function values in previous generations of data. The optimization problem can be written as:

$$\begin{aligned} \underset{x_1 \ldots x_5, J}{\text{minimize}} \quad & \eta\%, 1/weight \\ \text{subject to} \quad & b_{il} \leq x_i \leq b_{iu}, \; i = 1, 2, 3, 4, 5 \\ & J_l \leq J \leq J_u, \end{aligned}$$

where, limits b_{il}, b_{iu} are lower and upper bounds for the geometric variables and J_l, J_u are lower and upper bounds for the current density as given in Table 2.2.

The GOSET algorithm creates combinations of variables from the above set. For each variable set, an FEA model is created to evaluate generator rated output efficiency and active material weight. Based on the objective values of efficiency and weight, fitness values are assigned to each generator

design. These results are returned to the GOSET algorithm, which provides the variables for the next iteration of the FEA simulation. An initial population size of 1600 generators and 50 generations with 80 generators in each population was used for this study. Assigned fitness values are used to obtain the pareto optimal curve over the generations specified for the optimization process [14]. Figure 2.6 shows the flow process for generating the pareto optimal front and evaluating the electromagnetic performance.

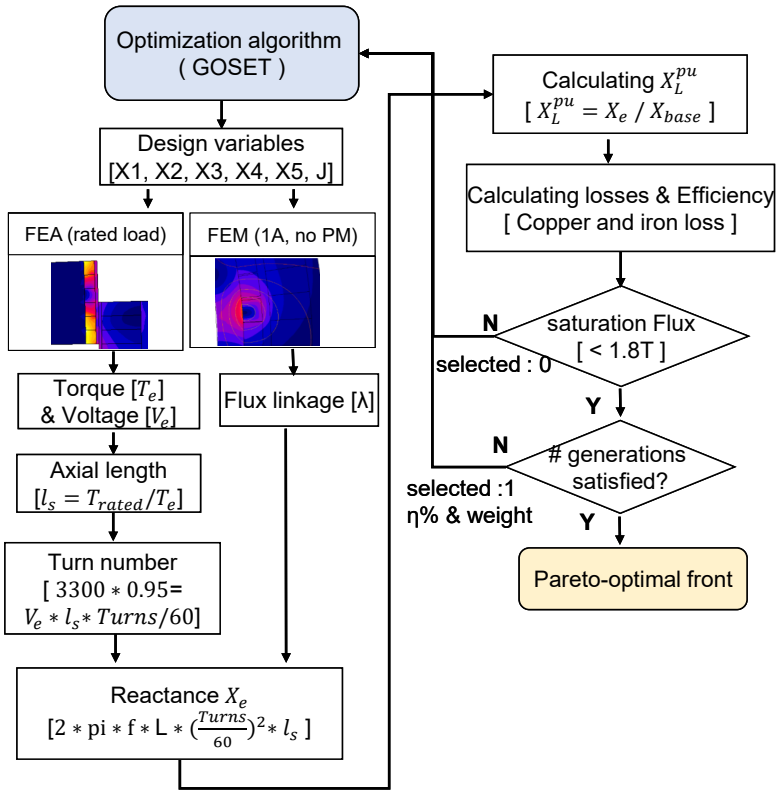

Figure 2.6: Flow process for generator design

During each iteration, a GOSET-generated variable set is fed into FEA software to perform two electromagnetic simulations: rated load simulation and inductance simulation. Rated load simulation evaluates the two objectives of efficiency and active material weight. The inductance simulation evaluates the per-unit reactance of each generator design. The results of per-unit reactance associated with each generator will be useful in the integration phase with power electronics, which will be discussed in chapter 3.

The rated load simulation only considers a unit length of the generator. The three main outputs from this simulation are peak phase voltage (V_e),

toque (T_e) per-unit length, and the flux density in the stator yoke (B_{sy}). Once the voltage and torque are obtained for the FEA model, the generator is then scaled by length to match the intended output torque as shown in Eq. 2.6 and Eq. 2.7.

$$T_{\text{rated}} = \frac{P_{\text{rated}}}{\omega_{rated}} = \frac{P_{\text{rated}}}{2\pi f_{\text{rated}}} \tag{2.6}$$

$$\text{axial length } (l_s) = \frac{T_{rated}}{T_e} \tag{2.7}$$

As the next step, the number of ampere-turns is determined. Since the diameter is large, number of turns is going to be very small for this generator. Thus, more resolution will be required, which can be done by having more parallel circuits. This was done by implementing 60 parallel circuits. The number of turns can be calculated as shown in Eq. 2.8 and Eq. 2.9, where $V_{l-l,rated}$ is the rated rms line voltage.

$$V_{e,new} = \frac{V_e l_s}{60} \tag{2.8}$$

$$\text{number of turns } (n) = \sqrt{\frac{2}{3}} \frac{V_{l-l,rated}}{V_{e,new}} \tag{2.9}$$

Once the data is obtained for torque, voltage, and flux density, the second FEA simulation is performed with 1A current in phase A of the generator. This was done after converting PM to inactive material. This captures the flux linkage (λ) under the 1A current supplied, which is the self inductance (L) of the phase-A winding. Since the machine is symmetric, all the windings will have the same value for self inductance. As the next step, per-unit reactance of the generator is calculated according to Eq. 2.10 and Eq. 2.11.

$$\text{Reactance } (X_L) = 2\pi f L (\frac{n}{60})^2 l_s \tag{2.10}$$

$$X_L^{pu} = \frac{X_L}{Z_{base}} \tag{2.11}$$

Efficiency calculation requires evaluating each loss component. Main loss components include copper loss, iron loss and friction loss in the bearings. The windage loss component can be neglected due to the very low speed

of rotation. Generator output efficiency can be calculated according to Eq. 2.12. For this study, a fixed loss of 10 kW is assumed.

$$\text{Generator efficiency } (\eta\ \%) = \frac{P_{out}}{P_{out} + loss_{cu} + loss_{iron} + loss_{fixed}} \tag{2.12}$$

Low speed generators used in wind turbine applications usually dominate in copper loss. In evaluating the copper loss, both active length and end winding length were considered due to the large diameter of the machine. Equation 2.13 was used to estimate the end-winding length, which makes use of pole-pitch length in calculation. Here, R_{cu} is the distance from the center of the rotor to the copper winding.

$$l_{end} = (\frac{2\pi R_{cu}}{\text{number of poles}})\frac{\pi}{2} \tag{2.13}$$

This design assumes two slots per-pole-per-phase. The area allocated for a single slot can be calculated using Eq. 2.14. Once the slot area is known, the fill factor and current density are used to calculate the current in the winding as shown in Eq. 2.15:

$$A_{cuA} = (\frac{\text{total copper area}}{\text{number of slots}}) \tag{2.14}$$

$$I_{rated} = A_{cuA}(\text{fill factor})J \tag{2.15}$$

The equivalent per-phase resistance of the circuit is a function of stack length and the end winding length. Thus, it can be calculated according to Eq. 2.16, where ρ is the resistivity of copper at 120 °C. With current and circuit resistance known, total copper loss can be calculated as in Eq. 2.17.

$$R_s = \frac{\rho(l_s + l_{end})}{A_{cuA}} \frac{\text{number of slots}}{3} \tag{2.16}$$

$$\text{Rated copper loss} = 3 * {I_{rated}}^2 * R_s \tag{2.17}$$

In a wind turbine, the generator does not always operate at rated speed. Thus, it is required to estimate partial load efficiency to understand energy production over time. Estimating the partial load copper losses was done using a simple assumption. Under maximum power point tracking to control

the turbine, the generator toque is proportional to the square of angular speed (ω^2) [15]. On the other hand, torque is directly proportional to current in a PM synchronous generator. Thus, copper loss is taken as a function of ω^4 as shown in Eq. 2.18:

$$\text{partial load copper loss} = \text{rated copper loss} * (\frac{\omega}{\omega_{rated}})^4 \tag{2.18}$$

Steinmetz hysteresis and eddy-current loss models are used for iron loss estimation. Stator yoke volume (V_{sy}) can be known from the dimensions being used for FEA simulation. With the stator iron volume known, loss coefficients of M235-35A is k_h and k_e are used to calculate total iron loss according to Eq. 2.19, where B_{sy} was obtained as a FEA result. The same equations can be used to calculate iron-loss at partial-loads by only changing the fundamental frequency based on the generator speed:

$$\text{iron loss} = (k_h f + k_e f^2) B_{sy}^2 V_{sy} \tag{2.19}$$

The selected material has a saturation flux density of 1.8 T. Thus, the designs which give a peak flux density above this maximum limit are not included in the study. As shown in the process flow of Fig. 2.6, if a flux density of more than 1.8 T detected, the process moves to the next design. Practically, this is done by assigning very low objective function values to make sure their attributes have a low probability in the next iteration. Designs which follow the flux density criteria return their objective functions of rated efficiency and 1/weight, which include them in the next iterations by GOSET algorithm.

The low inductance requirement for the generator was established based on power electronics integration. Thus, a maximum limit for X_L^{pu} of 0.15 was assumed. Figures 2.7 to 2.9 show the results for generator topology I after filtering based on the assumed X_L^{pu} limit. Figure 2.7 shows the rated efficiency versus the generator active weight with the color bar representing X_L^{pu} of each generator design. The target efficiency level of 97% and active material weight of 124.3 tons which corresponds to a torque density of 80 Nm/kg, are also marked in the plot to show the space where generator designs satisfy both conditions. Evidently, a slotless generator with Halbach array magnets can easily achieve the targets of efficiency and torque density while

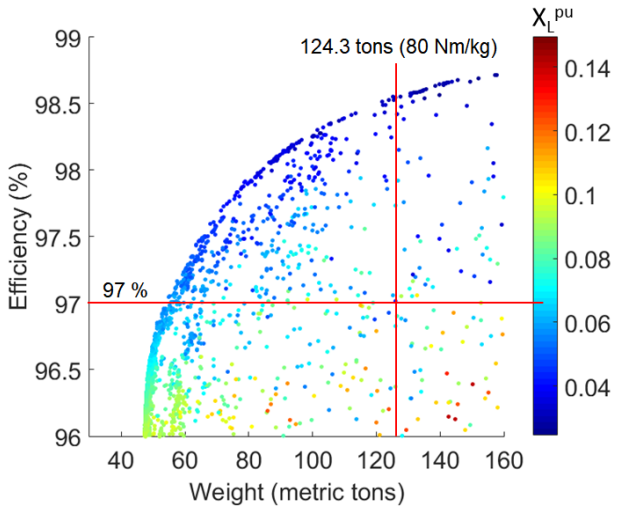

Figure 2.7: Rated efficiency vs. active weight of slotless generator with X_L^{pu} map

Table 2.3: Cost allocation for active materials

PM (NdFeB)	Copper	Iron
95 \$/kg	4.78 \$/kg	0.50 \$/kg

maintaining the X_L^{pu} below 0.15. A simple cost calculation was done for the generators based on active materials used. This calculation only includes the cost for PM, iron and copper as shown in Table 2.3 [7].

The same results are presented in Fig. 2.8, where color shows the cost for active materials. It can be seen that, to achieve both targets, the cost of the generator active material will be in a wide range between \$1.5-7 million. To compare the cost with a conventional machine, a reference design was created for the 10 MW PMSG in [7] using the same tools that were used for this study. The active material cost for reference design was found to be close to \$0.55 million, which is very low compared to the slotless generator topology that has been studied. The reference design had a rated efficiency of 93.5 % and had a X_L^{pu} of 0.45. This high X_L^{pu} is a result of the slotted-stator design and radial magnet arrangement with rotor back-iron, which reduces reluctance in the magnetic circuit.

Slotless topology uses thicker magnets compared to the conventional generator, to compensate for the increased effective airgap. This is one of the main reasons for low X_L^{pu} that is required for power electronics integration. This comparison gives the interesting insight that same slotless structure with a

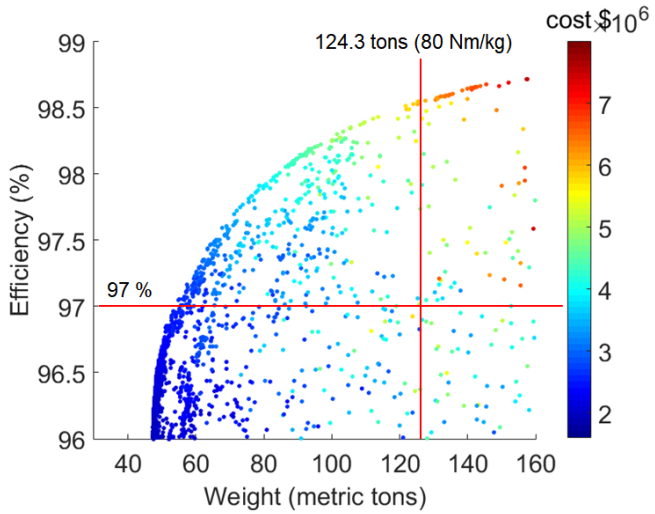

Figure 2.8: Rated efficiency vs. active weight of slotless generator with active material cost map

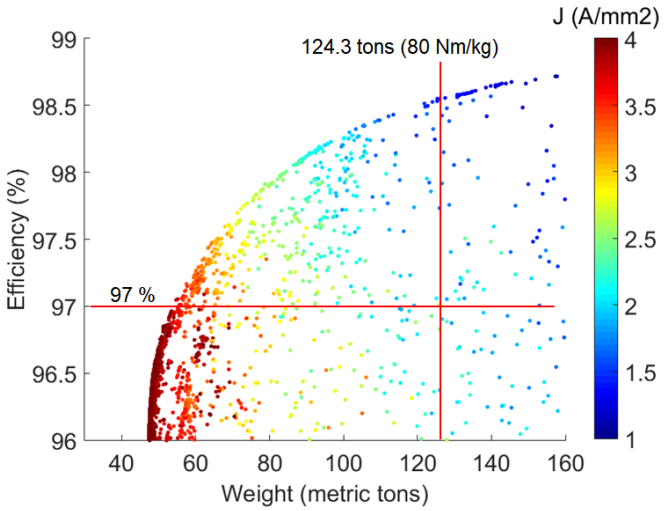

Figure 2.9: Rated efficiency vs. active weight of slotless generator with current density map

lower rated efficiency requirement can be cost competitive to a conventional design, as can be seen along the pareto curve in Fig. 2.8.

Figure 2.9 shows an interesting view on X_L^{pu}, by highlighting the current density on the color bar. Along the pareto front, the two extremes represent two different methods of achieving the terminal voltage. High efficiency designs along the pareto front becomes heavy designs with thicker magnets. This reduces the number of turns and as was discussed, X_L^{pu} is proportional to the square of the turns number. Having a lower number of turns enforces

lower current density in the slots, which reduces copper loss and increases efficiency. In low efficiency points along the pareto front, high numbers of turns are employed with thinner magnets, which increases X_L^{pu} but reduces the weight. From a practical generator design perspective, a design with lower current density is preferred, as it reduces the stress on the cooling system. However, according to the results shown, a trade-off exists between the efficiency, weight, X_L^{pu}, current density, and cost. The system level advantage is a function of annual energy production and cost of generator. One way to evaluate it is by using levelized cost of energy (LCOE). However, calculations of detailed system level indicators will not be performed under the scope of this study.

From the results of generator topology I, it was clear that the high generator cost was a result of high usage of magnets. Thus, alternative topologies are required, which targets to minimize the cost. One alternative is to use ferrite magnets, which has a low remnant flux density (B_r) compared to Nd-FeB magnets. Taking the B_r of ferrite magnets as 0.36 T, the generator requires either a thicker layer of magnets or a longer stack length to generate the same torque. Additional thickness in magnets further increases the effective airgap, which makes the generator heavier. Thus, a slotted stator architecture was employed, which reduces the effective airgap compared to a slotless generator. This may influence to increase X_L^{pu}. In addition to using a slotted stator to maintain a low stator weight, a Halbach array of magnets is used to minimize the rotor weight.

Figure 2.10 shows the cross section used for optimization process of this topology, while maintaining the same general assumptions. Variable limits used for the optimization process are shown in Table 2.4. Knowing the relatively low B_r, magnet thickness limit is increased up to 110 mm.

Table 2.4: Constraints used in optimization of generator topology II

Variable	Lower bound	Upper bound
Shaft radius X1 (mm)	5000	6000
Rotor yoke thickness X2 (mm)	30	200
Magnet thickness X3 (mm)	20	110
Slot depth X4 (mm)	25	100
Slot width/2 X5(mm)	2.5	10
Stator yoke thickness X6 (mm)	10	60
Current density J (A/mm2)	1	4

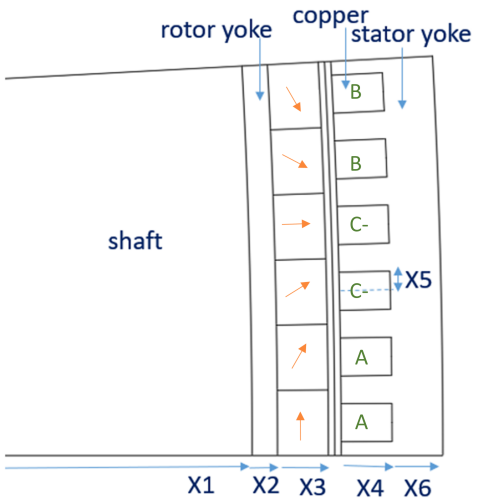

Figure 2.10: Geometric variables used for optimization of generator topology II

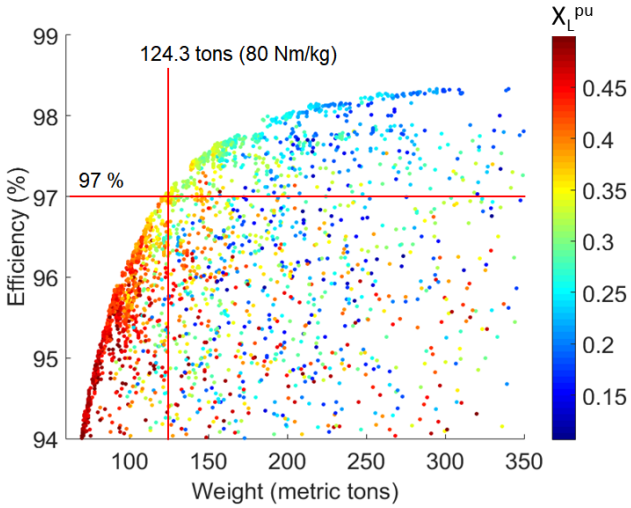

Figure 2.11: Rated efficiency vs. active weight of slotted ferrite generator with X_L^{pu} map

Results for this topology are shown in Fig. 2.11 and Fig. 2.12. Achieving a low X_L^{pu} is difficult with this topology as seen from the results. Thus, the plot shows all the designs below X_L^{pu} of 0.5. Still few designs can be found within the population, which has a X_L^{pu} below 0.15.

Compared to set targets for efficiency and torque density, only a few points meet both targets. As expected, the generator cost is much lower compared to the first topology, with a large number of designs falling below \$0.6 millions generator cost.

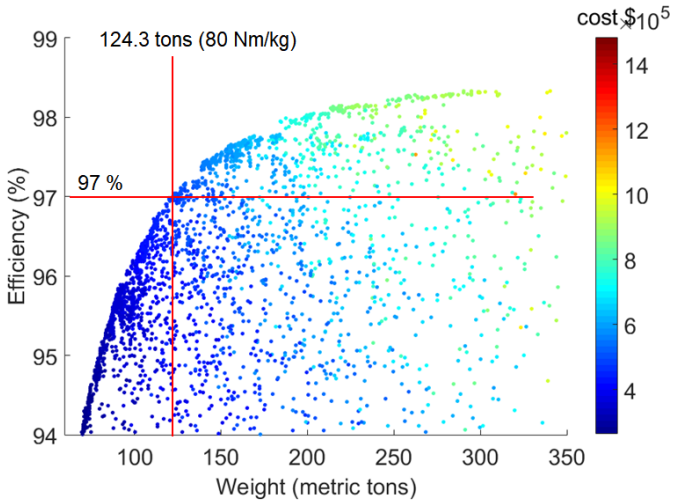

Figure 2.12: Rated efficiency vs. active weight of slotted ferrite generator with active material cost map

Although the cost is low, the topology II with ferrite magnets barely meets the efficiency and torque density targets. This was a result of weak remnant flux density in ferrite magnets. For the third topology, a conventional PM generator with NdFeB magnets was selected. This includes a slotted stator, radial NdFeB magnets and rotor back iron in contrast to the topology I. The cross section used in the optimization process is shown in Fig. 2.13. Since radial magnet orientation was used, the active material weight of this generator topology includes the weight of the rotor yoke, which is made of the same iron material as the stator. Limits for the optimization process are shown in Table 2.5.

Table 2.5: Constraints used in optimization of generator topology III

Variable	Lower bound	Upper bound
Shaft radius X1 (mm)	5000	6000
Rotor yoke thickness X2 (mm)	30	200
Magnet thickness X3 (mm)	10	50
Slot depth X4 (mm)	25	100
Slot width/2 X5(mm)	2.5	10
Stator yoke thickness X6 (mm)	10	60
Current density J (A/mm2)	1	4

Results for this generator topology is shown in Fig. 2.14 and Fig. 2.15. In terms of set targets, generator topology provides a reasonable range of designs. The cost can seen to be relatively lower compared to topology I.

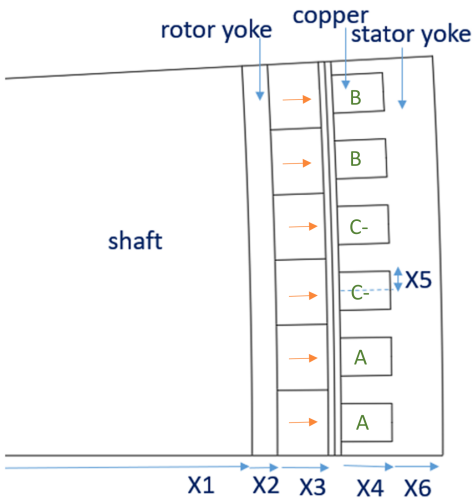

Figure 2.13: Geometric variables used for optimization of generator topology III

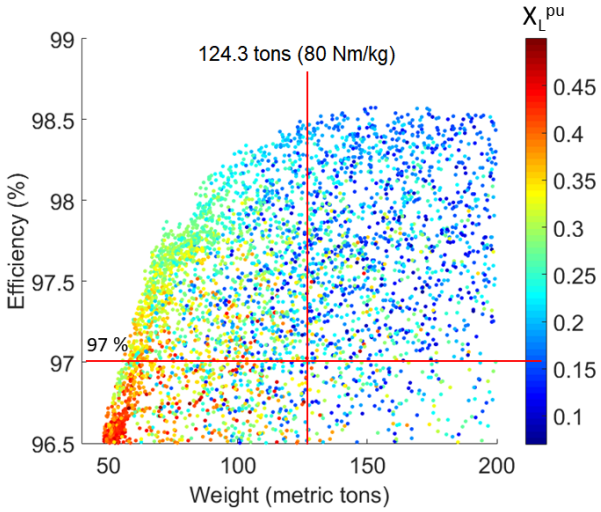

Figure 2.14: Rated efficiency vs. active weight of slotted (radial magnet) generator with X_L^{pu} map

There is a good design space with X_L^{pu} below 0.15. Thus, both topologies I and III provide a reasonable design space under given objectives. Topology II barely meets the targets for the efficiency and the torque density. At the same time, it also has a higher X_L^{pu} compared to the other two.

Pareto fronts for the three generator topologies are shown in Fig. 2.16. As can be seen, topologies I and III show a similar trend on rated efficiency and weight capability. However, the compatibility with proposed power electronic configuration for two topologies is different due to difference in X_L^{pu}.

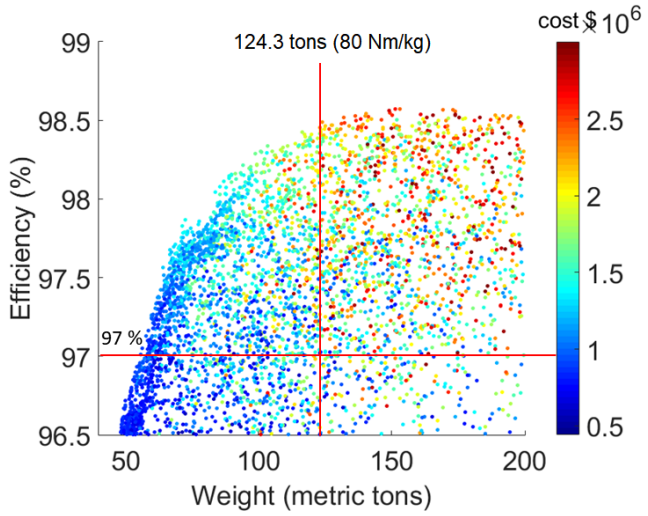

Figure 2.15: Rated efficiency vs. active weight of slotted (radial magnet) generator with active material cost map

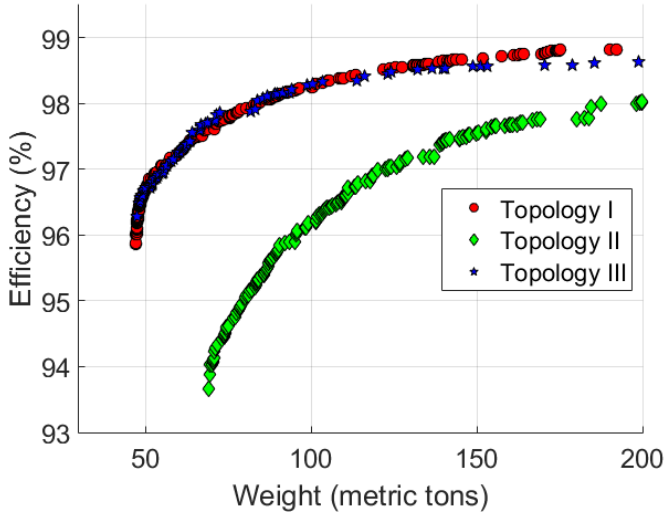

Figure 2.16: Pareto curves for rated efficiency vs. active weight of three generator topologies

Topology II can reach a reasonable level of efficiency, but with a heavier design compared to the other two topologies.

CHAPTER 3

POWER ELECTRONICS INTEGRATION

3.1 Background of Drive Architecture

Having obtained the results for three generator topologies, final selection of generator type depends on a detailed evaluation of generators at system level. However, as the X_L^{pu} plays a major role in compatibility. As system level comparison will not be performed in this study, the study will be extended with a selected topology, with provision to change the topology later. Thus, extended modeling will be done for the topology I, as it provides the lowest X_L^{pu}, while also meeting the efficiency and torque density targets.

Achieving maximum power point tracking (MPPT) with the proposed architecture shown in Fig. 3.1 is described in [16].

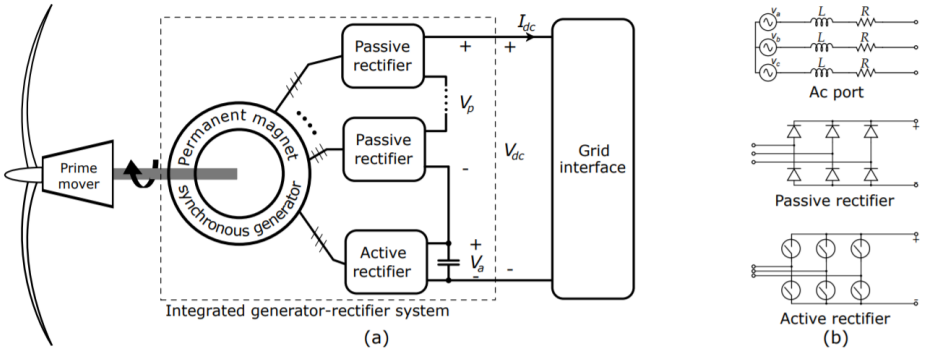

Figure 3.1: a). Multiport PMSG with integrated generator-rectifier system and b). Equivalent circuit for each port, active and passive rectifiers [16]

It provides the derivation of voltages in active and passive ports as given in Eq. 3.1 to Eq. 3.3.

$$V_a = V_{dc} - V_p \tag{3.1}$$

$$V_p = (k-1)(\frac{3}{\pi}(\sqrt{3}E(\omega) - I_{dc}\omega L) - 2RI_{dc}) \tag{3.2}$$

$$V_a = V_{dc} - (k-1)(\frac{3}{\pi}(\sqrt{3}E(\omega) - I_{dc}\omega L) - 2RI_{dc}) \tag{3.3}$$

Where, k refers to the number of ports and voltage drops ωLI_{dc}, RI_{dc} corresponding to synchronous reactance and phase equivalent resistance. As can be seen, when synchronous reactance increases, sum of voltage drops across passive ports. This forces more voltage to be handled by the active port. Thus, increased inductance in windings increase the stress on active rectifier. Figure 3.2 shows this effect for three different values of X_L^{pu}. As can be seen, increased synchronous inductance forces active rectifier to compensate for an increased voltage.

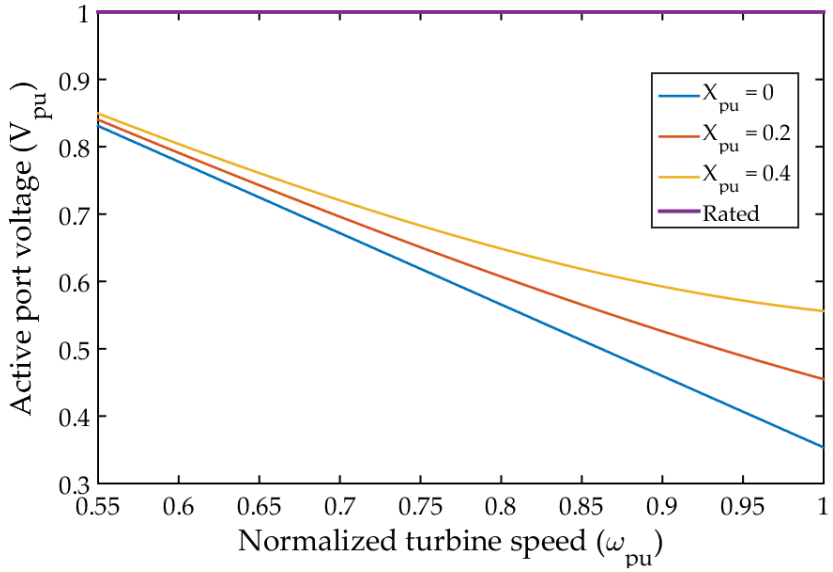

Figure 3.2: Effect on active rectifier voltage due to increasing X_L^{pu}

According to the results shown in [16], generator ports need to develop a counter-electromotive force (back-emf) waveform that is shifted by an angle to minimize the voltage ripple. The number of ports is decided based on the voltage ripple that can be allowed. Figure 3.3 shows the change in voltage ripple with phase shifted back-emf and Fig. 3.4 shows the reduction in voltage ripple with increasing passive ports. For this study, a combination of three passive ports with one active port is selected as it gives a reasonably low

voltage ripple.

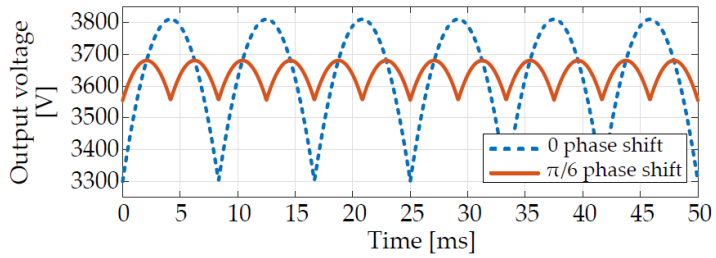

Figure 3.3: Expected back-emf phase shift for the drive integration [16]

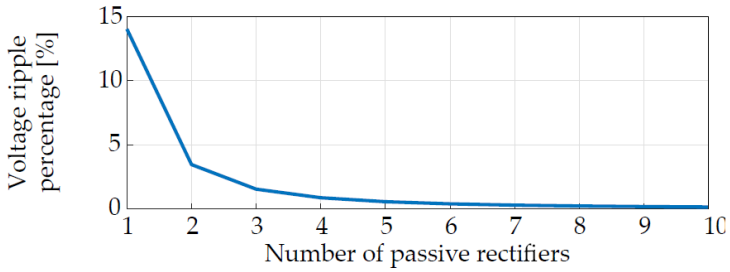

Figure 3.4: Number of passive ports vs. voltage ripple [16]

3.2 Winding Configuration

With the number of active and passive ports finalized, the generator windings can be designed in multiple ways. A common practice that is seen in wind generator drives is dividing the generator power into multiple modular drives. However, given the port configuration required in this case, division can be done in two main ways.

One way is to place all the active ports adjacent to each other and all the passive ports adjacent to each other. Second method would be to place four pole pair combinations (three passive ports and one active port) in a repetitive fashion along the stator circumference. The latter gives an advantage of minimizing the imbalance forces. This imbalance force is a result of imbalanced currents in active versus passive ports as shown in the example of Fig. 3.5. It shows difference in power processed between a conventional versus proposed technology with three ports applied to a 3 MW wind generator.

As can be noticed, at low speeds, a higher percentage of power is processed in the active port. This means passive ports carry less current and can give

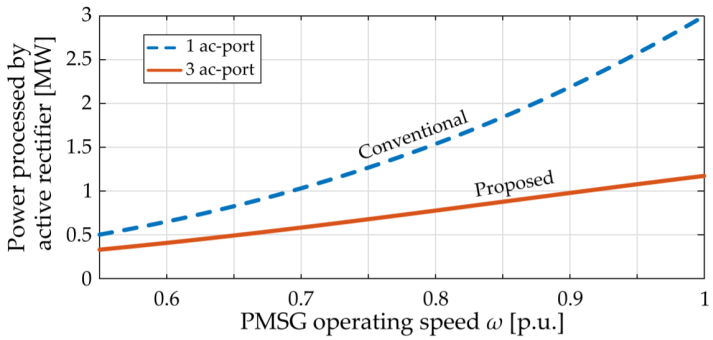

Figure 3.5: Power processed by active port in conventional vs. proposed architecture for a 3 MW wind generator [3]

rise to an imbalanced force if all the active ports were placed together in the stator. Thus, repeating the four pole pair combinations can minimize it.

In addition to the power sharing among ports, the same phase voltage among two passive ports should be shifted by $\pi/3(k-1)$ degrees (20°) to minimize voltage ripple [16]. In order to satisfy this requirement, the optimized generator model has to be modified with nine slots per pole. However, for slotless generator (topology I), it does not make a significant change to the electromagnetic performance. This was verified by comparing the performance of six slots per-pole vs. nine slots per-pole generator FEA models. With nine slots, the model will use the same copper area per phase with more turns. Therefore, changing the number of windings by a factor of 2/3, the same electromagnetic design can be obtained.

An FEA model was developed with eight poles, where six poles were assigned to passive ports and two poles to active port as shown in Fig. 3.6. It only contains eight poles of the machine, which represents $1/30^{th}$ of full symmetric machine. This reduced order eight pole model is used for FEA simulations.

Based on the requirement to control voltage ripple, a 20° degree phase shift between the back-emf of the same phase windings of passive ports has to be maintained. The final winding configuration is shown in Appendix A.

3.3 Results

With the FEA model developed, it was possible to verify the phase shift expected in the windings as shown in Fig. 3.7. As can be seen, A1, B1, and

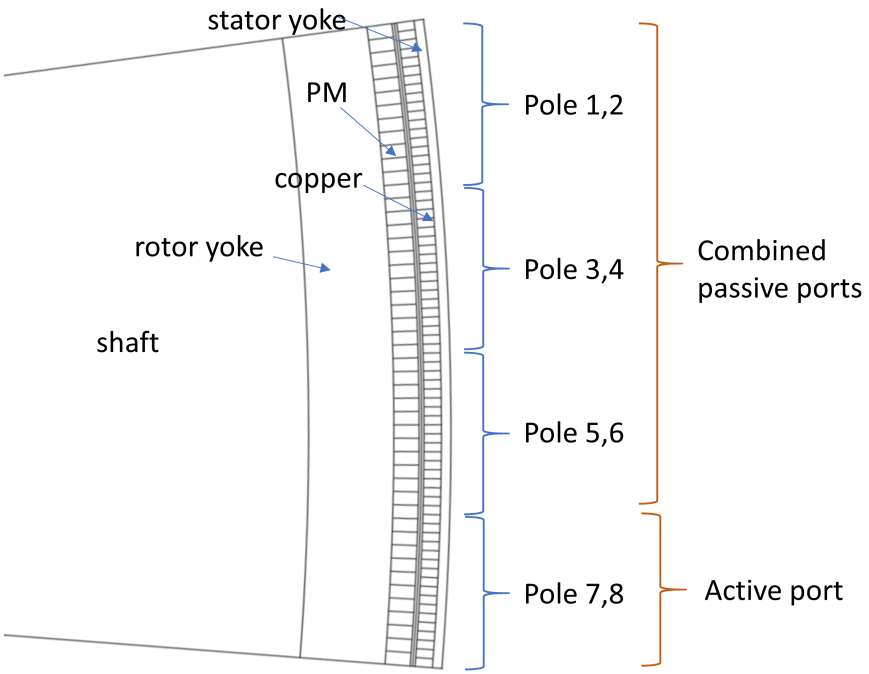

Figure 3.6: Winding assignment for the generator based on 8 pole symmetry

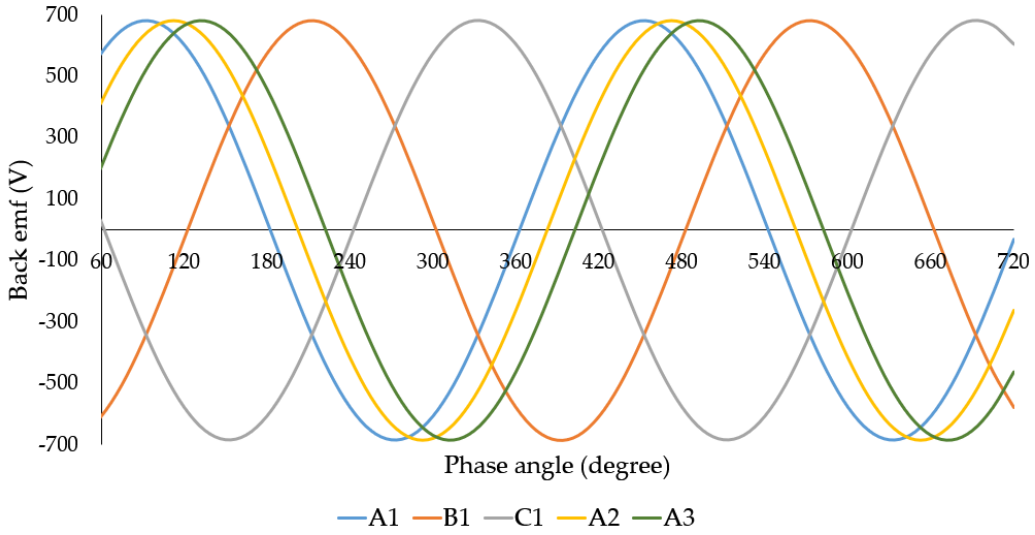

Figure 3.7: Phase shift between back-emf waveforms

C1 are shifted by 120° degrees as expected. In addition, each phases has two other windings in remaining passive ports, which are shifted to the main phase winding by 20° degrees. The active port should be switched in a way to make the passive port current be DC.

Previously for obtaining back-emf waveform, an open circuit model was used. However, implementing the actual circuit with diodes for passive ports

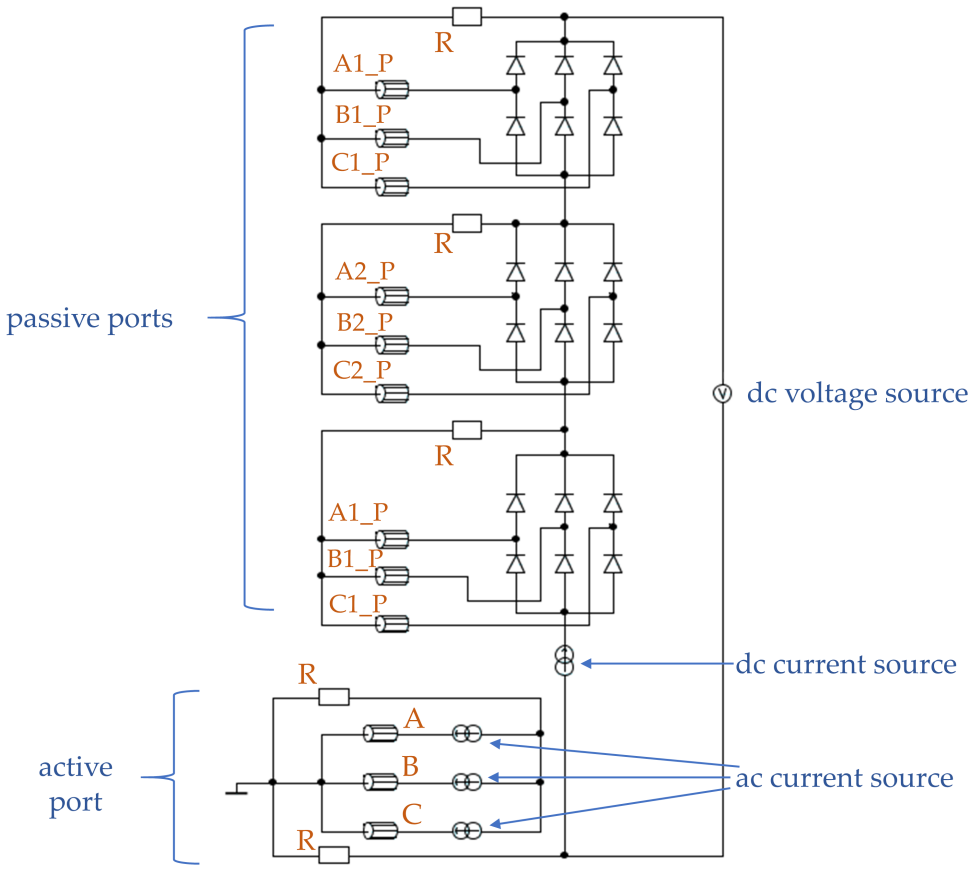

Figure 3.8: Circuit to imitate the equivalent circuit for FEA

and active switching is challenging due to its highly memory intensive process. Thus, a simplified circuit is implemented for the FEA model to simulate the loaded condition. Figure 3.8 shows the equivalent implementation of the circuit.

Here, the active port is supplied with current sources to overcome the challenges with implementation. A dc current source is connected in series with the passive circuit, such that it mimics the expected current, while a dc voltage source on the terminals mimic the zero voltage ripple condition. Importance in the consideration of X_L^{pu} or the synchronous inductance can be seen in this circuit. The voltage phase shift of 20° and current phase shift of 20° between the two ports of the same phase coil should be maintained for torque production. However, each coil conductor introduces an inductance to its current part, which causes commutation. Figure 3.9 shows the resultant current though coil conductors. As shown, they reasonably follow the voltage

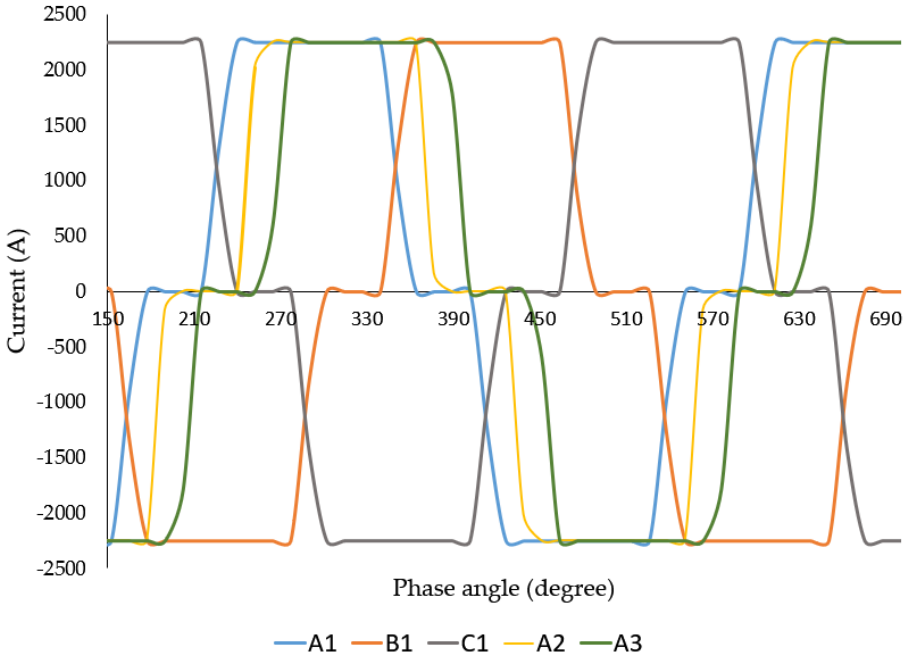

Figure 3.9: Resultant current through coil conductors

waveform with slope representing the series impedance due to inductance. Finally, Fig. 3.10 shows the electromagnetic torque output for this generator. Even though a ripple is present it is only 2.1% of the average torque.

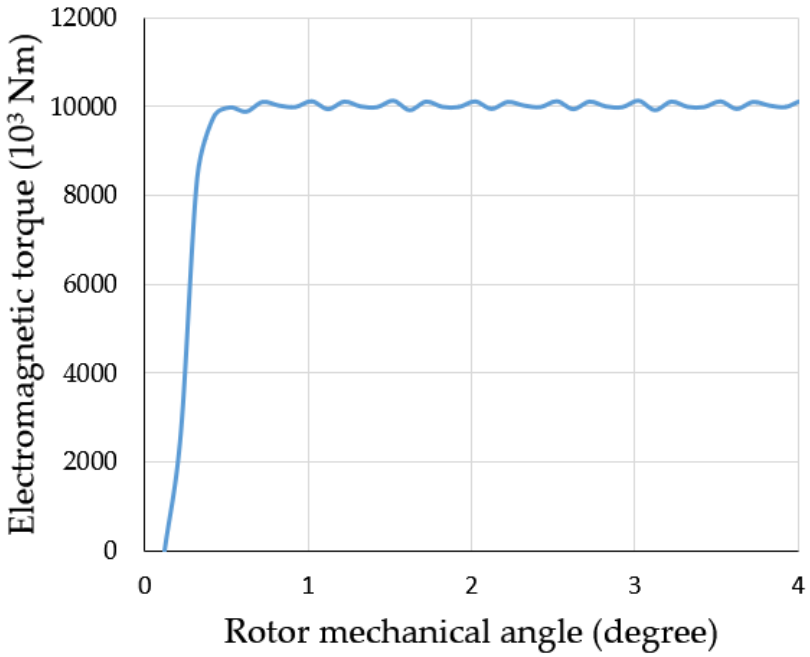

Figure 3.10: Output torque of the generator

CHAPTER 4

CONCLUSION

This thesis describes the trade-study, design and simulation results of a 10 MW direct drive PMSG for off-shore wind application with reduced cost for power electronics. In order for the generator-drive concept to be feasible, a low X_L^{pu} generator is necessary. Chapter 2 describes the process of designing and comparing the three generator topologies. In addition to comparing the efficiency and weight performance of three generator topologies, active material cost and X_L^{pu} were analyzed. Chapter 3 describes detailed design of the generator-drive system in order to achieve the final results. Results of FEA simulations for voltage waveforms, current waveforms and torque are presented.

Overall, this confirms the feasibility of this concept to dramatically reduce power electronics cost. The importance of inductance in coil conductors is discussed to achieve the intended targets. Even though the generator cost has increased compared to the conventional case, increased efficiency can increase annual energy production. Similarly, reduced electrical sub-system weight can reduce the tower cost. Thus, further investigation into control and system economics of this concept can validate the overall performance of suggested generator-drive sub-system. Future work also includes investigating the feasibility of this concept on conventional, relatively high inductance generators with measures to mitigate current commutation.

REFERENCES

[1] C. Bak, F. Zahle, R. Bitsche, T. Kim, A. Yde, L. C. Henriksen, M. H. Hansen, J. P. A. A. Blasques, M. Gaunaa, and A. Natarajan, "The DTU 10-MW reference wind turbine," in *Danish Wind Power Research 2013*, 2013.

[2] "Wind energy database." [Online]. Available: http://www.thewindpower.net/

[3] P. T. Huynh, P. J. Wang, and A. Banerjee, "An integrated permanent-magnet-synchoronous generator-rectifier architecture for limited-speed-range applications," *IEEE Transactions on Power Electronics*, vol. 35, no. 5, pp. 4767–4779, May 2020.

[4] D. Lee, A. Yoon, S. Sirimanna, S. Salon, and K. S. Haran, "Impact of manufacturing tolerances on a low reactance slotless PM synchronous machine," *IEEE Transactions on Energy Conversion*, vol. 35, no. 1, pp. 366–374, March 2020.

[5] C. C. Pavel, R. Lacal-Arantegui, A. Marmier, D. Schuler, E. Tzimas, M. Buchert, W. Jenseit, and D. Blagoeva, "Substitution strategies for reducing the use of rare earths in wind turbines," *Resources Policy*, vol. 52, pp. 349–357, 2017.

[6] H. Polinder, D. Bang, R. Van Rooij, A. McDonald, and M. Mueller, "10 mw wind turbine direct-drive generator design with pitch or active speed stall control," in *2007 IEEE International Electric Machines & Drives Conference*, vol. 2. IEEE, 2007, pp. 1390–1395.

[7] L. Sethuraman, M. Maness, and K. Dykes, "Optimized generator designs for the DTU 10-MW offshore wind turbine using GeneratorSE," in *35th Wind Energy Symposium*, 2017, p. 0922.

[8] Y. Duan and R. G. Harley, "Present and future trends in wind turbine generator designs," in *2009 IEEE Power Electronics and Machines in Wind Applications*, June 2009, pp. 1–6.

[9] K. O. Merz, "Dogger bank reference wind power plant: Layout, electrical design, and wind turbine specification," SINTEFF Energy Research, Tech. Rep., 2016.

[10] M. Ragheb, "Modern wind generators," *NetFiles, University of Illinois at Urbana–Champaign*, vol. 2, p. 28, 2014.

[11] R. Thurston, "Transactions of the American Society of Mechanical Engineers," *Science*, vol. 12, no. 312, pp. 964–965, 1900.

[12] W. Teng, R. Jiang, X. Ding, Y. Liu, and Z. Ma, "Detection and quantization of bearing fault in direct drive wind turbine via comparative analysis," *Shock and Vibration*, vol. 2016, 2016.

[13] X. Yi, "Electromagnetic-thermal modeling for high-frequency air-core permanent magnet motor of aircraft application," Ph.D. dissertation, 2016. [Online]. Available: http://hdl.handle.net/2142/95407

[14] S. Sudhoff, "Genetic Optimization System Engineering Tool (GOSET) for use with MATLAB, Manual Version 2.4, School of Electrical and Computer Engineering, Purdue University, West Lafayette, IN with United States Naval Academy, Annapolis, MD, 2005."

[15] M. A. Abdullah, A. Yatim, C. W. Tan, and R. Saidur, "A review of maximum power point tracking algorithms for wind energy systems," *Renewable and Sustainable Energy Reviews*, vol. 16, no. 5, pp. 3220–3227, 2012.

[16] P. Huynh, S. Tungare, and A. Banerjee, "Maximum power point tracking for wind turbine using integrated generator-rectifier systems," in *2019 IEEE Energy Conversion Congress and Exposition (ECCE)*, Sep. 2019, pp. 13–20.

APPENDIX A

WINDING LAYOUT

	Winding	Port
Pole 1,2	-B2	P3
	-B2	P2
	-B2	P1
	+C2	P3
	+C2	P2
	+C2	P1
	-A2	P3
	-A2	P2
	-A2	P1
	+B2	P3
	+B2	P2
	+B2	P1
	-C2	P3
	-C2	P2
	-C2	P1
	+A2	P3
	+A2	P2
	+A2	P1
Pole 3,4	-B1	P3
	-B1	P2
	-B1	P1
	+C1	P3
	+C1	P2
	+C1	P1
	-A1	P3
	-A1	P2
	-A1	P1
	+B1	P3
	+B1	P2
	+B1	P1
	-C1	P3
	-C1	P2
	-C1	P1
	+A1	P3
	+A1	P2
	+A1	P1

	Winding	Port
Pole 5,6	-B3	P3
	-B3	P2
	-B3	P1
	+C3	P3
	+C3	P2
	+C3	P1
	-A3	P3
	-A3	P2
	-A3	P1
	+B3	P3
	+B3	P2
	+B3	P1
	-C3	P3
	-C3	P2
	-C3	P1
	+A3	P3
	+A3	P2
	+A3	P1
Pole 7,8	-B3	Active port
	-B2	
	-B1	
	+C3	
	+C2	
	+C1	
	-A3	
	-A2	
	-A1	
	+B3	
	+B2	
	+B1	
	-C3	
	-C2	
	-C1	
	+A3	
	+A2	
	+A1	

Figure A.1: Winding assignment considering power sharing and voltage phase shift